Bayesian inference of neural connectivity in a population of neurons from calcium imaging data

(Dated: August 3, 2009)

We present Bayesian framework for inferring connectivity in a network of coupled neurons, observed simultaneously using calcium imaging.

Contents

I. MOTIVATION

Since Ramon y Cajal discovered that the brain is not a syncytium, but rather a rich and dense *network* of neurons, neuroscientists have wondered about the details of these networks. Since then, while much has been learned about "macro-circuits" — the connectivity between populations of neurons — relatively little is known about "micro-circuits" — the connectivity within populations of neurons. Broadly, one can imagine two distinct strategies for inferring microcircuit connectivity: anatomical and functional.

Anatomical approaches, while perhaps the gold standard for questions of connectivity, are often exceedingly laborious. Historically, neuroanatomists used tracing studies to address these questions, i.e., filled individual neurons with various dyes, and looked where the axons and dendrites terminated [?]. Besides being problematic with respect to whether the dyes filled the processes to the far proximal limit, or merely until the diameter became too small [?], this process is tedious and very low throughput. Recently, experimentalists have developed fluorescent proteins that express throughout the dendritic tree [?] or axonal arborization [?], that potentially resolves the premature termination issue, but not the throughput issue. Complementary to these labeling ideas, others have been developing Electron Microscopy based strategies to slice up neural tissue [?], and then automate track tracing using sophisticated image processing software [?]. This strategy has great promise for improving the throughput of these neuroanatomical studies, but have not yet quite achieved "off-the-shelf" status for experimental neuroscientists. Combining these powerful microscopy/computational tools with the genetic sensors, is perhaps the most promising emerging technology to date, but would still require hundreds to thousands of computational hours to infer the microcircuit for even small populations of neurons, such as part of a retina [?].

While these neuroanatomical approaches are under development, complimentary functional approaches are also rapidly improving. For instance, calcium-sensitive fluorescent indicators provide a glimpse into the spiking activity of

neurons, in a relatively non-invasive manner [**?**]. Very recently, some indicators achieve signal-to-noise ratios (SNRs) yielding single spike resolution [**?**]. In combination with these dyes, bulk-loading techniques enable experimentalists to simultaneously fill populations of neurons with such dyes [**?**]. While these approaches are state-of-the-art in terms of SNR, their invasiveness is a significant drawback. To that end, genetically encoded calcium indicators are under rapid development from a number of groups, and they are approaching SNR levels of nearly single spike accuracy as well [**?**]. Regardless of the source of the fluorescence, microscopy technologies for collecting the signal are also rapidly developing. Cooled CCDs for wide-field imaging (either epifluorscence or confocal) now achieve a quantum efficiency of $\approx 90\%$ with frame rates easily exceeding 30 or 60 Hz [**?**]. For in vivo work, 2-photon laser scanning microscopy can achieve similar frame rates, by designing software to efficiently control the typical scanners [**?**], using acoustic-optical deflectors to focus light at arbitrary locations in (three-dimensional) space [**?**], or using resonant scanners [**?**]. Together, these experimental tools can provide movies indicating calcium based fluorescent transients for small populations of neurons (e.g., $O(10^2)$), with "reasonable" SNR, at 30 Hz, both in the in vitro and in vivo scenarios.

Given these experimental advances in functional neural imaging, the stage is set for the development of complementary computational tools. To that end, we set out to build an algorithm that optimally utilizes the information provided by the above-described movies, to learn the most likely functional connectivity matrix governing the spiking of the observable neurons. Specifically, we develop an embedded-chain-within-blockwise-Gibbs approach, initialized using a sequential Monte Carlo method, and then relax some of our model assumptions to derive an efficient approximation that works well in practice. The result is that we can infer a large fraction of the variance of the functional connection matrix between a population of observable neurons, assuming realistic distribution of parameters for each neuron, and noise statistics. As our algorithm is inherently parallelizable, we run our program on a cluster of computers. For simulations and real data, in practice, given fluorescence traces from ≈ 100 neurons, total run time is approximately 10 minutes.

II. METHODS

A. Model

We first describe a parametric generative model that characterizes the statistics of the (unobserved) joint spike trains of all N observable neurons, along with the observed calcium fluorescence data. Each neuron is modeled as a generalized linear model (GLM); this class of model is known to capture the statistical firing properties of the of individual neurons fairly accurately [6, 7, 10, 21, 29–31, 33, 34, 37, 42, 46, 47]. We denote the i-th neuron's activity at time t as $n_i(t)$: in continuous time, $n_i(t)$ could be modeled as an unmarked point process, but we will take a discrete-time approach here, and so $n_i(t)$ will be a binary random variable. We model the spiking probability of neuron i via an instantaneous nonlinear function, $f(\cdot)$, of the filtered and summed input to that neuron at that time, $J_i(t)$. The input is composed of: (i) some baseline value, b_i; (ii) some external stimulus, $S(t)$, that is linearly filtered by k_i; and (iii) spike history terms, $h_j(t)$, from each neuron j, weighted by w_{ij}:

$$n_i(t) \overset{iid}{\sim} \text{Bernoulli}\big(f\big(J_i(t)\big)\big), \qquad J_i(t) = b_i + k_i \cdot S(t) + \sum_{j=1}^{N} w_{ij} h_j(t). \qquad (1)$$

To ensure computational tractability, we must impose some reasonable constraints on the instantaneous nonlinearity $f(\cdot)$ (which plays the role of the inverse of the link function in the standard GLM setting) and on the dynamics of the spike-history effects $h_j(t)$. More specifically, first, we restrict our attention to functions $f(\cdot)$ which ensure the concavity of the spiking loglikelihood in this model [30], as we will discuss at more length below. In this paper, we use

$$f(J) = P[X > 0 | X \sim Poiss(e^J \Delta)] = 1 - \exp[-e^J \Delta] \qquad (2)$$

(where the inclusion of Δ, the time step size, ensures that the firing rate scales properly with respect to the time discretization), though in our experience the results depend only weakly on the details of $f(\cdot)$ within the class of log-concave models [23, 30]; see [15] for a proof that this $f(\cdot)$ satisfies the required concavity constraints.

Second, because the algorithms we develop below assume Markovian dynamics, we model the spike history terms as:

$$h_j(t) = (1 - \Delta/\tau_h)h_j(t - \Delta) + n_j(t) + \sigma_h \sqrt{\Delta}\epsilon_j^h(t), \qquad (3)$$

where τ_h is the decay time constant for spike history terms, σ_h is a standard deviation parameter, $\sqrt{\Delta}$ ensures that the statistics of this Markov process have a proper Ornstein-Uhlenbeck limit as $\Delta \to 0$, and throughout this paper,

ϵ denotes an independent standard normal random variable. Note that this model generalizes (via a simple augmentation of the state variable $h_j(t)$) to allow each neuron to have several spike history terms, each with a unique time constant, which when weighted and summed allow us to model a wide variety of possible post-synaptic effects, including bursting, facilitating, and depressing synapses; see [48] for further details. In this paper, for simplicity, we assume that τ_h and σ_h are known synaptic parameters, and therefore our model spiking parameters θ^n are given by $\{\theta_i^n\}_{i=1}^N$, where $\theta_i^n = \{\mathbf{w}_i, k_i, b_i\}$, with $\mathbf{w}_i = (w_{i1}, \ldots, w_{iN})$.

The problem of estimating the connectivity parameters $\mathbf{w}_i$ in this type of GLM, given a fully-observed ensemble of neural spike train $\{n_i(t)\}$, has recently received a great deal of attention; see the references above for a partial list. In the calcium fluorescent imaging setting, however, we do not directly observe spike trains; $\{n_i(t)\}$ must be considered a hidden variable here. Instead, each spike in a given neuron leads to a rapid increase in the intracellular calcium concentration, which then decays slowly due to various cellular buffering and extrusion mechanisms. We in turn make only noisy, indirect, and subsampled observations of this intracellular calcium concentration, via fluorescent imaging techniques XXX ADD SOME BIOPHYSICAL CITES HERE XXX. To perform statistical inference in this setting, [48] proposed a simple conditional first-order hidden Markov model (HMM) for the intracellular calcium concentration $C_i(t)$ in cell i at time t, along with the observed fluorescence $F_i(t)$:

$$C_i(t) = C_i(t - \Delta) + (C_i^b - C_i(t - \Delta))\Delta/\tau_i^c + A_i n_i(t) + \sigma_i^c \sqrt{\Delta} \epsilon_i^c(t), \tag{4}$$

$$F_i(t) = \alpha_i S(C_i(t)) + \beta_i + \sqrt{\gamma_i S(C_i(t)) + \sigma_i^F} \epsilon_i^F(t). \tag{5}$$

This model can be interpreted as a simple driven autoregressive process: under nonspiking conditions, $C_i(t)$ fluctuates around the baseline level of C_i^b, driven by normally-distributed noise $\epsilon_i^c(t)$ with standard deviation $\sigma_i^c \sqrt{\Delta}$. Whenever the neuron fires a spike, $n_i(t) = 1$, causing the calcium variable $C_i(t)$ to jump by a fixed amount A_i, and subsequently decay with time constant τ_i^c. The fluorescence signal $F_i(t)$ corresponds to the count of photons collected at the detector per neuron per imaging frame. This photon count may be modeled with normal statistics, with the mean and variance given by generalized Hill functions, where $S(C) = C/(C + K_d)$ [49]. Because the parameter K_d effectively acts as a simple scale factor, and is a property of the fluorescent indicator, we assume throughout this work that it is known.

To summarize, Eqs. (1) – (5) define a coupled HMM: the underlying spike trains $n_i(t)$ and spike history terms $h_i(t)$ evolve in a Markovian manner, driving the intracellular calcium concentrations $C_i(t)$, which are themselves Markovian, but evolving at a slower timescale τ_i^c. Finally, we observe only the fluorescence signals $\{F_i(t)\}$, which are related in a simple Markovian fashion to the calcium variables $C_i(t)$.

B. Goal and general strategy

Our primary goal is to estimate the connectivity matrix, $\mathbf{w}$, given the observed set of calcium fluorescence signals $\mathbf{F}$. We must also deal with a number of nuisance parameters: the spiking parameters $\{k_i, b_i\}$ and the calcium parameters $\{C_i^b, \tau_i^c, A_i, \sigma_i^c, \alpha_i, \beta_i, \gamma_i, \sigma_i^F\}$. We addressed the problem of estimating these latter parameters in earlier work [48]; thus our focus here will be on $\mathbf{w}$. A Bayesian approach is natural here, since we have a good deal of prior information about neural connectivity; see [37] for a related discussion. However, a fully-Bayesian approach, in which we numerically integrate over the very high-dimensional parameter $\theta = \{\mathbf{w}, k_i, b_i, C_i^b, \tau_i^c, A_i, \sigma_i^c, \alpha_i, \beta_i, \gamma_i, \sigma_i^F\}$, is not particularly attractive here, from a computational point of view. Thus we take a compromise approach and compute *maximum a posteriori* (MAP) estimates for the parameters via an expectation-maximization (EM) algorithm in which the sufficient statistics are computed by a hybrid blockwise Gibbs sampler and sequential Monte Carlo (SMC) method.

More specifically, we iterate the steps:

E step: Evaluate $Q(\theta^{(l+1)}, \theta^{(l)}) = E_{P[\mathbf{X}|\mathbf{F};\theta^{(l+1)}]} \log P\left[\mathbf{F}, \mathbf{X}|\theta^{(l)}\right] = \int P[\mathbf{X}|\mathbf{F}; \theta^{(l+1)}] \log P[\mathbf{F}, \mathbf{X}|\theta^{(l)}] d\mathbf{X}$

M step: Solve $\theta^{(l+1)} = \underset{\theta}{\operatorname{argmax}} \left\{ Q(\theta, \theta^{(l)}) + \log P(\theta) \right\}$,

where $\mathbf{X}$ denotes the set of all hidden variables $\{C_i(t), n_i(t), h_i(t)\}_{i \le N, t \le T}$ and $P(\theta)$ denotes a (possibly improper) prior on the parameter space θ. According to standard EM theory [11, 24], each iteration of these two steps is guaranteed to increase the log-posterior $\log P(\theta^{(l+1)}|\mathbf{F})$, and will therefore lead to at least a locally maximum a posteriori estimator.

Now our major challenge is to evaluate the auxiliary function $Q(\theta^{(l+1)}, \theta^{(l)})$ in the E-step. Because our model is a

coupled HMM, as discussed in the previous section, Q simplifies considerably [35]:

$$
\begin{aligned}
Q(\theta, \theta^{(l)}) = & \sum_{it} P[C_i(t)|\mathbf{F}; \theta] \times \log P[F_i(t)|C_i(t); \alpha_i, \beta_i, \gamma_i, \sigma_i^F] \\
& + \sum_{it} P[C_i(t), C_i(t-\Delta), n_i(t)|\mathbf{F}; \theta] \times \log P[C_i(t)|C_i(t-\Delta), n_i(t); C_i^b, \tau_i^c, A_i, \sigma_i^c] \\
& + \sum_{it} P[n_i(t), \mathbf{h}(t)|\mathbf{F}; \theta] \times \log P[n_i(t)|\mathbf{h}(t); b_i, k_i, \mathbf{w}_i, S(t)],
\end{aligned}
\tag{6}
$$

where $\mathbf{h}(t) = \{h_i(t)\}_{i=1}^N$. Thus we need only compute low-dimensional marginals of the full posterior distribution $P[\mathbf{X}(t)|\mathbf{F}; \theta]$; specifically, we need pairwise marginals, of the form $P[X_i(t), X_i(t-1)|\mathbf{F}; \theta]$. The high dimensionality of the hidden variable $\mathbf{X}$ necessitates the development of specialized blockwise Gibbs-SMC sampling methods, as we describe in sections II C and II D below. Once we have obtained these marginals, the M-step breaks up into a number of independent optimizations that may be computed in parallel and which are therefore relatively straightforward (section II E); see section II F for a pseudocode summary along with some specific implementation details.

C. Initialization of "internal" parameters via sequential Monte Carlo methods

We begin by constructing relatively cheap, approximate preliminary estimators for the nuisance parameters $\theta \backslash \mathbf{w}$ (i.e., all of the parameters except the connectivity matrix $\mathbf{w}$; that is, all of the parameters which are "internal" to neuron i). The idea is to initialize our estimate $\theta^{(0)}$ by assuming that each neuron is observed independently. Thus we want to compute $P[X_i(t), X_i(t-\Delta)|\mathbf{F}_i; \theta_i]$, and solve the M-step for each individual parameter θ_i, with the connection matrix $\mathbf{w}$ held fixed. This single-neuron case is much simpler, and has been discussed at length in [48]; therefore, we only provide a brief overview here. The standard forward and backward recursions provide these posteriors [39]:

$$
P[X_i(t)|F_i(0:t)] \propto P[F_i(t)|X_i(t)] \int P[X_i(t)|X_i(t-\Delta)]P[X_i(t-\Delta)|F_i(0:t-\Delta)]dX_i(t-\Delta)
\tag{7}
$$

$$
P[X_i(t), X_i(t-\Delta)|F_i] = P[X_i(t)|F_i] \frac{P[X_i(t)|X_i(t-\Delta)]P[X_i(t-\Delta)|F_i(0:t-\Delta)]}{\int P[X_i(t)|X_i(t-\Delta)]P[X_i(t-\Delta)|F_i(0:t-\Delta)]dX_i(t-\Delta)},
\tag{8}
$$

where we have dropped the conditioning on the parameters θ for brevity's sake. Because these integrals cannot be analytically evaluated for our model, we approximate them using SMC ("marginal particle filtering") methods [13, 14, 18]; see [48] for details on the proposal density and resampling methods used here. The output of these SMC techniques comprise an array of particle positions $\{X_i^{(l)}(t)\}$, where l indexes the particle number, and a discrete approximation to the marginals $P[X_i(t), X_i(t-\Delta)|F_i]$,

$$
P[X_i(t), X_i(t-\Delta)|F_i] \approx \sum_{j,l} r_i^{(j,l)}(t, t-\Delta)\delta\left[X_i(t) - X_i^{(l)}(t)\right] \times \delta\left[X_i(t-\Delta) - X_i^{(j)}(t-\Delta)\right],
\tag{9}
$$

where $r_i^{(j,l)}(t, t-\Delta)$ denotes the weight attached to the particle pair with positions $\left(X_i^{(l)}(t), X_i^{(j)}(t-\Delta)\right)$.

As discussed above, the sufficient statistics for estimating the parameters for each neuron, θ_i, are exactly these marginal posteriors. As shown in Eq. (6), the M-step decouples into three independent subproblems. The first term depends on only $\{\alpha_i, \beta_i, \gamma_i, \sigma_i\}$; since $\log P[F_i(t)|C_i(t); \theta_i]$ is quadratic (by our Gaussian assumption on the fluorescent observation noise), we can estimate these parameters by solving a weighted regression problem (specifically, we use a coordinate-optimization approach: we solve a quadratic problem for $\{\alpha_i, \beta_i\}$ while holding $\{\gamma_i, \sigma_i\}$ fixed, then estimate $\{\gamma_i, \sigma_i\}$ by the usual residual error formulas while holding $\{\alpha_i, \beta_i\}$ fixed). Similarly, the second term requires us to optimize over $\{\tau_i^c, A_i, C_i^b\}$ using a quadratic solver, and then we use the residuals to estimate σ_i^c. Note that all the parameters mentioned so far are constrained to be non-negative, but may be solved efficiently using standard quadratic program solvers. Finally, the last term, assuming neurons are independent, may be expanded:

$$
E[\log P[n_i(t), \mathbf{h}_i(t)|\mathbf{F}; \theta]] = P[n_i(t), h_i(t)|F_i] \log f(J_i(t)] + (1 - P[n_i(t), h_i(t)|F_i]) \log[1 - f(J_i(t))];
\tag{10}
$$

since $J_i(t)$ is a linear function of $(b_i, k_i, \mathbf{w}_i)$, and the right-hand side of (10) is concave in $J_i(t)$, we see that the third term in (6) is a sum of terms which are concave in $(b_i, k_i, \mathbf{w}_i)$, and may therefore be solved efficiently using any convex optimization method, e.g. Newton-Raphson or conjugate gradient ascent.

Our procedure therefore is to initialize the parameters for each neuron using some default values that we have found to be effective in practice, and then recursively (i) estimate the marginal posteriors (E step), and (ii) maximize the

parameters (M step), using the above described approach. We iterate these two steps until the change in parameters does not exceed some minimum threshold. We can then use the marginal posteriors from the last iteration to seed the blockwise Gibbs sampling procedure described below, to obtain a rough estimate of $P[\mathbf{h}(t)|\mathbf{F}]$.

D. Estimating joint posteriors over weakly coupled neurons

Now we turn to the key problem: computing $P(\mathbf{h}(t), n_i(t)|F, \theta)$, which encapsulates the sufficient statistics for estimating the connectivity matrix $\mathbf{w}$ (recall equation (6)). The SMC methods described in the preceding section only provide the marginals over each neuron, $P[X_i(t)|F_i; \theta_i]$; these methods may in principle be extended to obtain the desired full posterior $P[\mathbf{X}(t)|\mathbf{F}; \theta]$, but since the SMC algorithm is fundamentally a sequential importance sampling method, these techniques scale poorly as the dimensionality of the hidden state $\mathbf{X}(t)$ increases [2]. Thus we need a different approach.

One very simple idea is to use a Gibbs sampler: sample sequentially from

$$X_i(t) \sim P[X_i(t)|\mathbf{X}_{\setminus i}, X_i(0), \dots, X_i(t - \Delta), X_i(t + \Delta), \dots, X_i(T), \mathbf{F}; \theta], \tag{11}$$

looping in some order over all cells i and all time bins t. Unfortunately, this approach is likely to mix very poorly, due to the strong temporal dependence between $X_i(t)$ and $X_i(t + \Delta)$. Instead, we propose to use a blockwise Gibbs strategy, sampling each spike train as a block:

$$X_i \sim P[X_i|\mathbf{X}_{\setminus i}, \mathbf{F}; \theta]; \tag{12}$$

if we can draw these blockwise samples $X_i = \{X_i(t)\}$ efficiently for a large subset of timebins t simultaneously, then we would expect the resulting Markov chain to mix much more quickly than the naive element-wise Gibbs chain, since by assumption the hidden variables X_i, X_j are weakly dependent for different cells $i \neq j$, and Gibbs is most efficient for weakly-dependent variables.

So, how can we efficiently sample from $P[X_i|\mathbf{X}_{\setminus i}, \mathbf{F}; \theta]$? One attractive approach is to try to repurpose the SMC methods described above, which are quite effective for drawing approximate samples from $P[X_i|\mathbf{X}_{\setminus i}, \mathbf{F}_i; \theta]$ for one neuron i at a time. Recall that sampling from an HMM is in principle easy by the "propagate forward, sample backward" method: we first compute the forward probabilities $P[X_i(t)|\mathbf{X}_{\setminus i}(0 : t), \mathbf{F}(0 : t); \theta]$ recursively for timesteps 0 up to T, then sample backwards from $P[X_i(t)|\mathbf{X}_{\setminus i}(0 : T), \mathbf{F}(0 : T), X_i(t + \Delta); \theta]$. This approach is powerful because each sample requires just linear time to compute (i.e., $O(T/\Delta)$ time, where T/Δ is the number of desired time steps). Unfortunately, in this case we can only compute the forward probabilities approximately (with the SMC forward recursion (7)), and so therefore this attractive forward-backward approach only provides approximate samples from $P[X_i|\mathbf{X}_{\setminus i}, \mathbf{F}; \theta]$, not the exact samples required to establish the validity of the Gibbs method.

Of course, in principle we should be able to use the Metropolis-Hastings (M-H) algorithm to correct these approximate samples. The problem is that the M-H acceptance ratio in this setting involves a high-dimensional integral over the set of paths that the particle filter might possibly trace out, and is therefore difficult to compute directly. [1] discuss this problem at more length, along with some proposed solutions. However, a slightly simpler approach was introduced by [27]. Their idea is to exploit the $O(T/\Delta)$ forward-backward sampling method by embedding a discrete Markov chain within the continuous state space $\mathcal{X}_t$; the state space of this discrete embedded chain is sampled randomly according to some distribution ρ_t with support on $\mathcal{X}_t$. It turns out that an appropriate acceptance probability (defined in terms of the original state space model transition and observation probabilities, along with the auxiliary sampling distributions ρ_t) may be computed quite tractably, guaranteeing that the samples produced by this algorithm form a Markov chain with the desired equilibrium density. See [27] for details.

We can apply this embedded-chain method quite directly here to sample from $P[X_i|\mathbf{X}_{\setminus i}, \mathbf{F}; \theta]$. The one remaining question is how to choose the auxiliary densities ρ_t. We would like to choose these densities to be close to the desired marginal densities $P[X_i(t)|\mathbf{X}_{\setminus i}, \mathbf{F}; \theta]$, and conveniently, we have already computed a good (discrete) approximation to these densities, using the SMC methods described in the last section. The algorithm described in [27] requires that ρ_t be continuous densities, so we simply convolve our discrete SMC-based approximation (specifically, the marginal of (9)) with an appropriate normal density to arrive at a very tractable mixture-of-Gaussians representation for ρ_t.

Thus, to summarize, our procedure for sampling from the desired joint state distributions $P(\mathbf{h}(t), n_i(t)|F, \theta)$ has a Metropolis-within-blockwise-Gibbs flavor, where the internal Metropolis step is replaced by the $O(T/\Delta)$ embedded-chain method introduced by [27], and the auxiliary densities ρ_t necessary for implementing the embedded-chain sampler are obtained using the SMC methods from [48].

1. A cheaper high-SNR approximation of the joint posteriors

If the SNR in the calcium imaging is sufficiently high, then by definition the observed fluorescence data F_i will provide enough information to exactly determine the underlying hidden variables X_i. Thus, in this case the joint posterior approximately factorizes into a product of marginals for each neuron i:

$$P[\mathbf{X}|\mathbf{F};\theta] \approx \prod_{i=1}^{N} P[X_i|F_i;\theta]. \tag{13}$$

We can take advantage of this representation because we have already estimated all the above marginals using the SMC methods described in section II C. In particular, we can obtain the sufficient statistics $P(\mathbf{h}(t), n_i(t)|\mathbf{F}, \theta)$ by forming a product over the marginals $P(X_i(t)|\mathbf{F}_i, \theta)$ obtained from (9). This approximation entails a very significant gain in efficiency for two reasons: first, it obviates the need to generate joint samples via the expensive blockwise-Gibbs approach described above; and second, because we can very easily parallelize the SMC step, inferring the marginals $P[X_i(t)|\mathbf{F}_i;\theta_i]$ and estimating parameters θ_i for each neuron on a separate processor. We will discuss the empirical accuracy of this approximation in more depth in the Results section.

E. Estimating the functional connectivity matrix

Computing the M-step for the connectivity matrix, $\mathbf{w}$, is an optimization problem with on the order of N^2 variables. By construction, however, the auxiliary function (6) is concave in $\mathbf{w}$, and decomposes into N terms which may be optimized independently using standard ascent methods. To improve our estimates, we will incorporate two sources of strong *a priori* information via our prior $P(\mathbf{w})$: first, prior anatomical studies have established that connectivity in many neuroanatomical substrates is "sparse," i.e., most neurons form synapses with only a fraction of their neighbors [3, 8, 16, 17, 20, 26, 32, 36, 40, 43], implying that many elements of the connectivity matrix $\mathbf{w}$ are zero; see also [30, 33, 37, 41] for further discussion. Second, "Dale's law" states that each of a neuron's postsynaptic connections in adult cortex (and many other brain areas) must all be of the same sign (either excitatory or inhibitory). Both of these priors are easy to incorporate in the M-step optimization, as we discuss below.

1. Imposing a sparse prior on the functional connectivity

Enforcing sparseness for signal recovered with a series of linear measurements via $L1$-regularizer is known to dramatically reduce the amount of data necessary to accurately reconstruct the signal [9, 12, 25, 28, 44, 45]. We incorporate a prior of the form $\log p(\mathbf{w}) = const. - \lambda \sum_{i,j} |w_{ij}|$, and additionally enforce the constraints $|w_{ij}| < m$, for a suitable constant m (since both excitatory and inhibitory cortical connections are known to be bounded in size). Since the penalty $\log p(\mathbf{w})$ is concave, and the constraints $|w_{ij}| < m$ are convex, we may still solve the resulting optimization problem in the M-step using standard convex optimization methods [4]. In addition, the problem retains its separable structure: the full optimization may be broken up into N smaller problems that may be solved independently.

2. Imposing Dale's law on the functional connectivity

Enforcing Dale's law requires us to solve a non-convex, non-separable problem: we need to optimize the concave function $Q(\theta, \theta^{(l)}) + \log P(\theta)$ under the non-convex, non-separable constraint that all of the columns of the matrix $\mathbf{w}$ are of a fixed sign (either nonpositive or nonnegative). It is difficult to solve this problem exactly, but we have found that simple greedy methods are quite efficient in finding good (possibly approximate) solutions. We begin with our original sparse solution, obtained as discussed in the previous subsection without enforcing Dale's law. Then we assign each neuron as either excitatory or inhibitory, based on the weights we have inferred in the previous step: i.e., neurons i whose inferred postsynaptic connections w_{ij} are largely positive are tentatively labeled excitatory, and neurons with largely inhibitory inferred postsynapic connections are labeled inhibitory. Neurons which are highly ambiguous may be unassigned in the early iterations, to avoid making mistakes from which it might be difficult to recover. Given the assignments a_i ($a_i = 1$ for putative excitatory cells, -1 for inhibitory, and 0 for neurons which have not yet been assigned) we solve the convex, separable problem

$$\underset{a_i w_{ij} \geq 0 \ \forall i,j}{\operatorname{argmax}} \ Q(\theta, \theta^{(l)}) + \log P(\theta), \tag{14}$$

which may be handled using the standard convex methods discussed above. Given the new estimated connectivities $\mathbf{w}$, we can re-assign the labels a_i, or even flip some randomly to check for local optima. We have found this simple approach to be fairly effective in practice.

F. Specific implementation notes

Pseudocode summarizing our approach is given in Algorithm 1. As discussed in section II C, the "internal" parameters $\theta \backslash \mathbf{w}$ may be initialized effectively using the methods described in [48]; then the full parameter θ is estimated via EM, where we use the embedded-chain-within-blockwise-Gibbs approach discussed in section II D (or the cheaper conditionally-independent approximation described in section II D 1) to obtain the sufficient statistics in the E step and the separable convex optimization methods discussed in section II E for the M step.

Algorithm 1 Pseudocode for estimating functional connectivity from calcium imaging data using EM; η^n, η^F, N_G are user-defined convergence tolerance parameters. XXX CAN WE INDENT THE BELOW PROPERLY? WOULD MAKE IT MORE LEGIBLE XXX

---

while $|\mathbf{w}^{(l)} - \mathbf{w}^{(l-1)}| > \eta^w$ **do**
  for all $i = 1 \ldots N$ **do**
    while $|\theta_i{}^{(l)} - \theta_i{}^{(l-1)}| > \eta^F$ **do**
      Approximate $P[X_i(t)|F_i; \theta]$ using SMC (section II C)
      Perform the M-step for the "internal" parameters $\theta \backslash \mathbf{w}$ (section II C)
    end while
  end for
  for all $i = 1 \ldots N$ **do**
    Approximate $P[n_i(t), \mathbf{h}(t)|\mathbf{F}; \theta]$ using either the blockwise Gibbs method or the high-SNR conditionally-independent approximation (section II D)
  end for
  for all $i = 1 \ldots N$ **do**
    Perform the M-step using separable convex optimization methods (section II E)
  end for
end while

As emphasized above, the parallel nature of these EM steps is essential for making these computations tractable. We performed the bulk of our analysis on a high-performance cluster of Intel Xeon L5430 based computers (2.66 GHz). For 10 minutes of simulated fluorescence data, imaged at 30 Hz, calculations typically took 10-20 minutes per neuron using the conditionally-independent approximation, with time split approximately equally between (i) estimating the internal parameters $\theta \backslash \mathbf{w}$, (ii) approximating the posteriors using the independent SMC method, and (iii) estimating the functional connectivity matrix, $\mathbf{w}$. The hybrid MCMC-Gibbs sampler was substantially slower, up to an hour per neuron per Gibbs pass, with the Gibbs sampler dominating the computation time. XXX IS THIS RIGHT? ONE HOUR PER NEURON? WHY IS EACH GIBBS SWEEP SO SLOW RELATIVE TO A PARTICLE FILTER SWEEP? XXX

G. Accuracy of the estimates and Fisher information matrix

XXX THIS SHOULD PROBABLY BE REDUCED A BIT AND MOVED TO THE RESULTS; BETTER TO EXPLAIN THE RESULTS AFTER WE ACTUALLY SHOW THEM XXX

To determine the necessary amount of data for accurate estimation of the functional connectivity matrix, we calculate Fisher information for $P[\mathbf{w}|\mathbf{X}]$. Assuming for simplicity perfect knowledge of spike trains (i.e. such not corrupted by inference errors from calcium imaging) and single time-bin coupling, i.e. $h_j(t) \neq 0$ only for time-delay $t = 1$, we write the Fisher information matrix as:

$$C^{-1} = \frac{\partial(-\ln P)}{\partial w_{ij} \partial w_{i'j'}} = - \delta_{ii'} \sum_t \left[n_i(t) n_j(t-1) n_{j'}(t-1) \left(-\frac{f'(J_i(t))^2}{f(J_i(t))^2} + \frac{f''(J_i(t))}{f(J_i(t))} \right) \right. \\ \left. - \Delta(1 - n_i(t)) n_j(t-1) n_{j'}(t-1) f''(J_i(t)) \right]. \tag{15}$$

where f' and f'' correspond to the first and second derivatives of our linking function (c.f Eq. (1)), and $\delta_{ii'}$ is XXX ? XXX. When $f(J) = \exp(J)$ XXX Y: we don't use an exponential here. is it worth modifying this accordingly? XXX, and coupling between spikes is week, this may be rewritten as:

$$C^{-1} = \delta_{ii'}(T\Delta)P[n_i(t) = 0, n_j(t-1) = 1, n_{j'}(t-1) = 1]E[f(J_i(t))|n_i(t) = 0, n_j(t-1) = 1, n_{j'}(t-1) = 1]$$
$$\sim (T\Delta)\left[(r\tau_w)\delta_{ii'}\delta_{jj'} + O((r\tau_w)^2)\right]r. \tag{16}$$

Here $(T\Delta)$ is the total observation time, τ_w is "the coincidence time" — the typical EPSP/IPSP time-scale over which the spike of one neuron affects the spike probability of the other neuron — and $r \approx E[f(J_i(t))|n_i(t) = 0, n_j(t-1) = 1, n_{j'}(t-1) = 1]$ is the typical firing rate. For successful determination of the functional connectivity matrix $\mathbf{w}$, the variance C should be smaller than the typical scale $\langle \mathbf{w}^2 \rangle$, i.e.

$$(T\Delta) \sim (\mathbf{w}^2 r^2 \tau_w)^{-1}. \tag{17}$$

For typical values of $\mathbf{w}^2 \approx 0.1$, $r \approx 5$ Hz and $\tau_w \approx 10$ msec, with this order of magnitude estimate we obtain T of the order of hundred seconds. This theoretical estimate of the necessary amount of fluorescent data is in good agreement with our simulations below.

Note also that necessary recording time does not depend on the number of neurons in the imaged network N. This unexpected result is the direct consequence of the special form of C^{-1} in Eq. (16). In particular, when $r\tau_w << 1$, this matrix is dominated by the diagonal term $(T\Delta)(r^2\tau_w)$, and so the Fisher information matrix is predominantly diagonal with the scale $(r^2\tau_w T\Delta)^{-1}$, independent of the number of neurons N. This theoretical result is also directly confirmed in our simulations below.

III. RESULTS

A. Simulating neural activity in a neural population

To test the described method for inferring functional connectivity from calcium imaging data, we simulated a network of stochastically connected neurons constructed as close as possible to resemble the real cortical microcircuits, based on experimental data available from the literature [5, 19, 22, 38]. We prepared sparse random networks of $N = 10 - 500$ neurons. Each neuron was modeled using Eqs. (1) and (3).

The network was divided into excitatory (80%) and inhibitory (20%) neurons [5, 19], each respecting Dale's law, i.e., all axons for a particular neuron were either excitatory or inhibitory (corresponding to all positive or all negative columns in our functional connection weight matrix, $\mathbf{w}$). Neurons were randomly connected to each other with probability 0.1 [5, 22]. Synaptic weights for excitatory connections, as defined by EPSP peak amplitude, were randomly drawn from exponential distribution with the mean of $0.5\mu V$ [22, 38]. These were then converted to GLM weights: while synaptic weights physiologically were measured in μV, in GLM functional connectivity weights were measured in log-rate units of Eq. (1)). GLM weights described the change in the probability of the neuron i to fire given neuron j had fired before, as opposed to physiologically measured injected currents or changes in membrane potential. By utilizing this definition, synaptic weights were converted into GLM weights assuming that each EPSP corresponded to added probability of neuron spiking in given time bin of $\Delta P = V_E/V_b$, where v_E is peak EPSP amplitude and V_b is the membrane resting potential below threshold (implying that V_b/V_E EPSPs would be required to trigger neuron over the threshold),

$$w_{ij} = \ln(-\ln(e^{-r_i\tau_w} - V_E/V_b)/r_i\tau_w), \tag{18}$$

where $r_i = \exp(b_i)$ is the base firing rate of neuron i and $\tau_w = 10$ msec was the typical EPSP/IPSP scale over which single EPSP affects the firing probability of the neuron i.

Inhibitory connections were also drawn from exponential distribution with the negative mean. Inhibitory connections strength was chosen so as to balance excitatory and inhibitory currents in the network and achieve an average firing rate of ≈ 5 Hz. Practically, the mean strength of inhibitory connections was about 10 times larger than that of the excitatory connections.

The time course of functional connectivity weights $w_{ij}(t)$ was modeled as the difference of two exponentials with the rise time of 1 msec and decay time of 10 msec for excitatory and 20 msec for inhibitory currents [38]. Up to 25% variation in these time constants could be allowed. We neglected conduction delays, given that the time delay below ~ 1 msec expected in local cortical circuit was smaller than the time step of our computer simulation. Additionally to excitatory and inhibitory currents, each neuron was modeled to have refractory current with the time-course described as an exponential with time constant of 10 ms.

Spike-trains were generated using GLM by simulating network forward in time with the time step of 1 ms. Given the spike rasters, the fluorescence observations were generated using calcium dynamics model Eq. (4). Parameters for the model were chosen according to our experience with few actual cells analyzed using algorithm of [48], see Table I. The population of cells was generated with these parameters allowing cell-to-cell variance of at least 30%. More specifically, each parameter was generated from a normal distribution with specified mean and variance at about 30% of the mean, truncated at the lower bound at about 30% of the mean value. Fluorescence was obtained for calcium imaging at the frame-rate of 33 Hz or 66Hz. From 300 sec to 3600 sec of calcium imaging data was simulated.

TABLE I: Table of simulation parameters.

Total neurons	10-500
Excitatory neurons	80%
Connections sparseness	10%
Baseline firing rate	5 Hz
Mean EPSP strength	0.5 μV
Mean IPSP strength	2.3 μV
EPSP profile	1 msec rise time, 10 msec decay time
IPSP profile	1 msec rise, 20 msec decay time
Mean Ca noise σ_c	28 μM
Mean Ca jump A_c	80 μM
Mean Ca background C_b	24 μM
Mean Ca decay time τ_c	0.25 sec
Mean photon budget α_c	1-80 Kph/neuron/frame
K_d	200 μM

B. Inference of the functional connectivity from the simulated calcium imaging data

With neural population activity prepared as described in the previous section, we used our Bayesian inference algorithm to reconstruct the functional connectivity matrix from simulated fluorescence data. Specifically, we calculated the connectivity matrix by solving the maximum likelihood problem Eq. (??),

$$E[\ln P_{\mathbf{n}}(n_i|\mathbf{n}_{\setminus i}; W)] = \sum_t \left(n_i(t) \ln J_i(t) - (1 - n_i(t)) \exp(J_i(t))\Delta \right), \qquad (19)$$

$$J_i(t) = b_i + \sum_j \sum_{t' < t} w_{ij}(t - t') n_j(t') = b_i + \sum_j w^{ij} h_j(t). \qquad (20)$$

The sum in Eqs.(19) and (20) was over the sample of $\{n_i(t)\}$, produced with our spike sampling algorithm, discretized over the time-bins t' with the width corresponding to the calcium imaging frame-rate (i.e. 30 ms for 33 Hz and 15 ms for 66 Hz). In one of the two cases we considered, EPSP time-profiles were assumed to be "known" exponential, and the weights were estimated using reduced histories $h_i(t) = \sum_{t' < t} \exp(-(t - t')/\tau_h) n_i(t')$ with the time constant $\tau_h = 10$ ms (i.e. second equation in Eq. (20)). In the second case we considered, the time dependence of $w_{ij}(t)$ was assumed to be unknown and the first equation in Eq. (20)) was used to correlate $n_i(t)$ with $n_j(t')$ for $t' < t$ up to a given depth m. In this latter case, since each next term in Eq. (20)) was significantly smaller than the previous one, we found that the best results were obtained if we took $m = 1$ (i.e. minimizing number of unknown variables given certain amount of data). In either case, we described the connection weight between two neurons by a scalar quantity $w_s^{ij} = \text{sign}(w_{ij}) \max_t |w_{ij}(t)|$, which thereafter was used to compare true and reconstructed connectivity weights in all examples below.

We performed reconstruction of functional connectivity from fluorescence data using MCMC-Gibbs algorithm as well as using independent approximation, Figure 3. We found that independent approximation algorithm was able to provide reconstructions almost as accurate as the exact MCMC-Gibbs algorithm for experimentally interesting imaging regimes. We therefore concluded that the independent approximation was essentially equivalent to the exact MCMC-Gibbs method for the purpose of functional connectivity reconstruction.

We then performed reconstruction of functional connectivity from the original (true) spike trains down-sampled at the frame-rates of calcium imaging. Fluorescence data is generally acquired at low frame-rate and, so, one of its
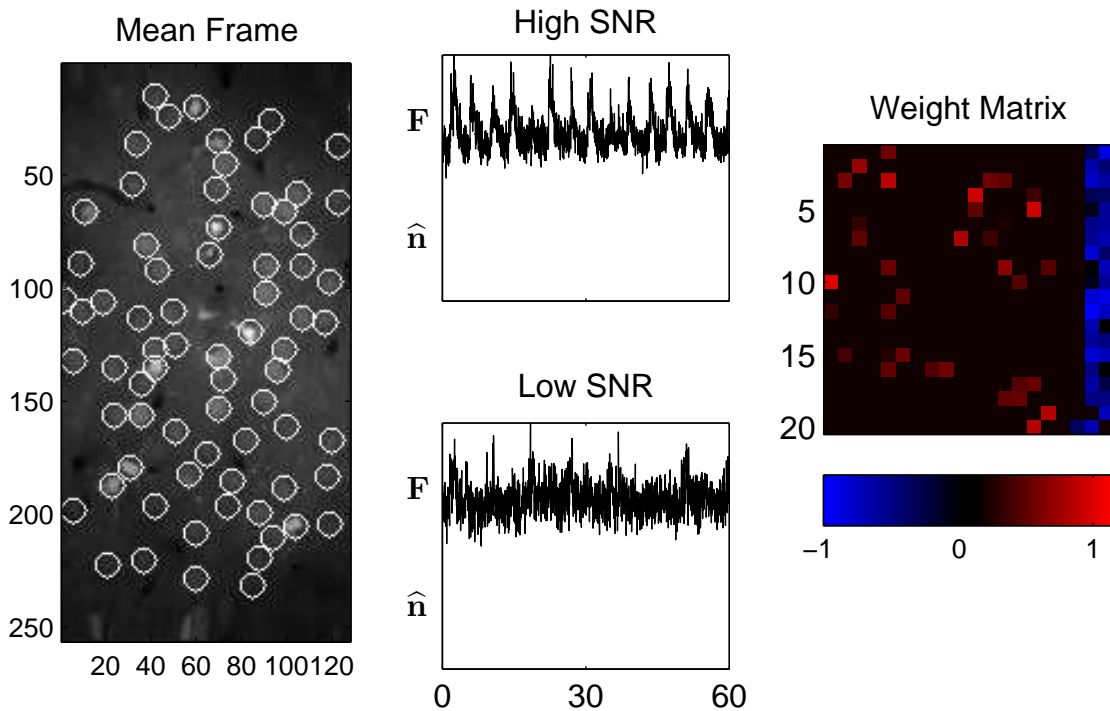
FIG. 1: A schematic depicting our data analysis pipeline. The left panel shows the mean image from an in vivo experiment, with regions-of-interest indicated by white circles, as determined by a custom algorithm (see Methods for details). By averaging the pixel intensity of all the pixels within a region of interest, we obtain a one-dimensional fluorescence trace for each neuron. The middle panel shows two such examples, the top showing a trace with relatively high signal-to-noise ratio (SNR), and the bottom showing a trace with a relatively low SNR. We use these signals to sample likely spike trains (below each trace), and use such joint spike trains to estimate the functional connectivity matrix, as shown in the left panel.
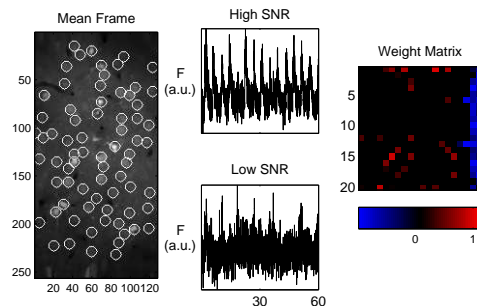
FIG. 2: In calcium imaging a population of neural cells is continuously imaged using light microscopy and calcium sensitive fluorescent indicator (left panel). Whenever a neuron generates an action potential (fire), calcium influx through cellular membrane leads to a change in the fluorescence of the dye, thus allowing to detect the moments when cell fires (central panels). Accurate identification of spike trains from calcium imaging data gives access to detailed functional connectivity matrices for populations of neurons as large as 1,000 - 10,000 of cells.

main limitations is bad time-resolution of the observed spike trains. To determine the impact of this constraint on the connectivity reconstructions, and, thus, to determine how close calcium imaging may approach reconstructions from spike trains directly observed under comparable conditions, we conducted this experiment. We observed that at intermediate SNR reconstructions from calcium imaging closely resembled such obtained directly from spike trains, and at higher SNR reconstruction with the quality same with original spike trains was achieved, Figure 3 and 6.

Our estimated connectivity matrix was always biased with respect to the true connectivity by a constant factor. The origin of this bias is the coarse time discretization of the spike trains inferred from calcium imaging, $\Delta \approx 15-30$ msec,

large on the scale of EPSP/IPSP time scale $\tau_w = 10 - 20$ ms. Really, if Δ is large, the first term in the sum Eq. (20) $w_{ij}(\Delta) \approx w_s^{ij} \exp(-\Delta/\tau_w)$ is substantially smaller than w_s^{ij} and connectivity weights estimated from GLM $w_{ji}(\Delta)$ will be scaled relative to w_s^{ij}. To estimate the magnitude of this scaling bias, we consider two neurons coupled by GLM weight w_{12}. w_{12} can be inferred by observing the number of spikes from the two neurons in excess of the baseline firing rate $\Delta n_{12} \approx \int dt w_{12} \exp(-t/\tau_w)$ (where we assumed exponential time course for $w_{12}(t)$). Now, assuming spike trains are discretized into bins of size $\Delta \sim \tau_w$, and assuming that we only dismiss all spike pairs occurred in the same time bins as coincident, the number of excess spike pairs observed empirically is $\Delta n'_{12} \approx \langle \exp(-\Delta/\tau_w) \rangle = \int_0^\Delta dt_1/\Delta \int_\Delta^\infty dt_2 \exp(-(t_2 - t_1)/\tau_w)$, where the average is understood over all spike pairs from consecutive time-bins. The ratio

$$\Delta n'_{12}/\Delta n_{12} = (1 - \exp(-\Delta/\tau_w))/(\Delta/\tau_w) \tag{21}$$

is the connectivity weights additional scaling due to the spike train time-discretization. In Figure 4 we plot the magnitude of this bias as computed from Eq.(21) versus that empirically observed in our simulations for different values of Δ. Simple theoretical estimate Eq.(21) accurately described the observed amount of bias in the estimated connectivity matrices.

Scaling bias in principle may be removed by performing inference of the spike trains with the bin size $\Delta \to 0$. However, we were not successful in performing this calculation. One problem that we encountered was the increased variance in the connectivity estimates. Since in Eq.(20) the coincident time bin $t = t'$ was omitted from the sum, all spike pairs within the same time-bins were removed from the GLM fit. Because time position of such spikes pairs, inferred from fluorescence data, typically had inaccuracy $\approx \Delta$, their temporal order often could be confused, thus, polluting GLM dataset. In Eq.(20) with $\Delta \approx 1$/frame-rate such spike pairs were automatically removed. However, if $\Delta \to 0$, such pairs would remain.

Consider now two neurons i and j. If the number of spikes of neuron i following neuron j within time-span Δ was n_{ij}, while such in the reverse order was n_{ji}, difference $\delta n_{ij} = n_{ij} - n_{ji}$ would correspond to the difference of GLM weights $\delta w_{ij} = w_{ij} - w_{ji}$. However, if such spike pairs inferred from calcium imaging had their order confused with probability $p \approx 1/2$, the number of spike pairs n_{ij} actually observed would become $n_{ij}(1-p) + n_{ji}p$, while that for the reverse order would become $n_{ji}(1-p) + n_{ij}p$, and empirically estimated difference $w_{ij} - w_{ji}$ would correspondingly drop to $\delta w'_{ij} = (1 - 2p)\delta w_{ij}$, while the variance would remain the same.

This effect complicated the problem of estimating the functional connectivity matrix W by effectively mixing w_{ij} and w_{ji}, and introducing large error in W estimates moving them toward the symmetrized version of W. For finer time-discretization the amount of data necessary to overcome this noise in W, due to disordering of closely positioned inferred spike-pairs, appeared to be well over ≈ 10 min of data used for the most of the calculations shown in this section below. Such high-time-resolution samples of spike trains also were substantially more computationally expensive to obtain and work with. For these reasons, we did not pursue this line of research further, although it may be of interest in the future.

What minimal conditions for the experimental calcium imaging setup should be met to allow successful reconstruction of the connectivity from calcium imaging data? In Figures 5-7 we answer this question. In Figure 5, the quality of the inferred connectivity matrix is shown as function of the imaging frame-rate: imaging frame rates 30-60 Hz are needed to achieve meaningful reconstruction results. These imaging frame-rates are feasible for already existing experimental setups. In Figure 6 the quality of the inferred connectivity matrix is shown as function of imaging SNR, as quantified by the photon budget of the experimental setup. From our experience with the analysis of real cells [48], the photon budget in real data was ~ 10 Kph/cell/frame for in-vivo data collected at 15 Hz and ~ 100 Kph/cell/frame for in-vitro data at the same frame-rate. As can be seen from Figure 6, the photon budget necessary for accurate reconstructions was 10-40 Kph/neuron/frame. For lower photon counts the amount of noise in calcium imaging data degraded inferred connectivity matrices significantly. In Figure 7 the quality of the inferred connectivity matrix is shown as function of the calcium imaging data amount from 5 min to 1 hour. The minimal necessary amount of data depended substantially on whether prior information about the distribution of connectivity weights was incorporated into the M-step. In particular, for M-step based on simple GLM, the calcium imaging duration necessary to achieve $r^2 = 0.5$ for the reconstructed connectivity matrix was $T \sim 10$ min, while for M-step solving sparse-GLM $r^2 > 0.5$ was achieved already at $T \sim 5$ min (assuming 5 Hz of firing rate). These numbers appear to be well within limitations of the existing experimental setups. Furthermore, in agreement with theoretical analysis in the Methods, the accuracy of the reconstruction did not depend on the size of imaged neural population, with the same reconstruction quality observed for the same amount of data for $N = 50 - 200$ neurons. In all cases, good reconstructions were obtained already with $T \sim 5 - 30$ min of calcium imagign data.

"Anatomical" connectivity was recovered in our experiments despite potential problems noted in the literature [XXX], e.g. such as common input from correlated neurons. This is primarily due to the particular form of the activity

in our neural networks, whereas firing of neurons occurred independently, thus, allowing GLM explore the full range of possible input configurations and disentangle common inputs.

Estimation of the functional connectivity is fundamentally routed in observing changes in the spike rate conditioned on the state of the other neurons. Intuitively, such estimation can be compared to observing changes in $p(\mathbf{n}(t)) = \exp(\sum_j w_{ij} n_j(t))$ for different neural configurations $\mathbf{n}(t)$, i.e. estimating a vector $\mathbf{w}_i$ from a number of dot-products $\mathbf{w}_i \cdot \mathbf{n}(t)$ with different vectors $\mathbf{n}(t)$. In order to properly estimate all components of $\mathbf{w}_i$ the set of available $\mathbf{n}(t)$ should be rich enough to span all N dimensions of $\mathbf{w}_i$. In case of independent firing such condition is clearly satisfied. Should this condition be violated, however, e.g. due to high correlation between spiking of few neurons, spike trains may not provide access to the complete vector $\mathbf{w}_i$, and the connection weights inferred from such activity data may effectively "aggregate" true connection weights in arbitrary linear combinations.

To empirically test the impact of this effect, we carried out a simulation of hypothetical "strongly" coupled neural network, where in addition to weak sparse connectivity we introduced sparse random strong connectivity component. In some sense, we allowed a fraction of neurons to couple strongly to the other neurons, thus making them "command" neurons "driving" activity of the other neurons. The strength of strong connectivity component was chosen to build up the actual firing rate dynamically from the baseline rate of $r = \exp(b) \approx 1$ Hz to ≈ 5 Hz.

Such neural network showed patterns of activity very different from the weakly coupled networks inspected above, Figure 8. In particular, large number of highly correlated, synchronously locked firings of many neurons were evident in this network. Likewise, our algorithm was not able to identify the true connectivity matrix correctly, Figure 8.

Our inference algorithm showed significant robustness to potential deviations of the real data from our generative model. One important distortion likely to occur in the real data is varying time-scales of EPSPs of different synapses. Such variability in τ_w would result in added variance in the estimated weights w_{ij} through τ_w dependence of the scaling factor Eq.(21). However, we found that such added variance to be insignificant in our simulations with τ_w varying for up to 25%, Figure 9.

Taking into account simple prior information about the connectivity matrix resulted in dramatic improvement of the inferred connectivity matrix. sparseness prior resulted in dramatic improvements allowing successful reconstruction from as little as 5 min of calcium imaging data, and allowing to achieve for $T \approx 10$ min the same level of accuracy that would otherwise require up to $T \approx 1$ hour of calcium imaging data, Figure 7 and 10. Dale's prior only led to 10% in the correlation coefficient r^2 of the reconstructed connectivity matrix, and was not found significant.

We applied our algorithm to a sample of the real calcium imaging data from [XXX], totaling about 5 minutes of imaging for a population of 72 cells in [XXX]. Out of these, about 23 cells had fluorescence traces indicative of spikes, while the other cells were either silent or did not shown SNR sufficient for analysis. These 23 cells were selected for futher processing. 20-200 spikes were found for each cell, corresponding to firing rates from 0.07 Hz to 0.8 Hz. We then identified functional connectivity matrix for this population. Sparse solution resulted in consistent connectivity matrix with sparseness of about 10%, automatically respecting Dale's law, and clearly indicating two strongly connected excitatory neurons and few inihibitory neurons. Although this data lacked independent controls necessary to properly evaluate quality of our obtained reconstruction, it does demonstrate that our approach can be successfully applied under real-life condition to analyze functional connectivity of real populations of neurons.

IV.   DISCUSSION

a.   j's outline of discussion   summary of main point: using sparse prior, we can recover a large fraction of variance of connection weights, assuming reasonable SNR, parameters, and imaging rate.

h_j vs. h_{ij} reduces dimensionality of hidden space to $O(N)$ vs. $O(N^2)$, leading to our approach scaling well as $N \to$ big

$P(A|BC) \neq P(A|B)P(A|C)$ unless B and C are uncorrelated. we use this property, correlation coefficient doesn't, cross-correlations, etc., do not.

for the same reason, hidden neurons might be a problem for us. faster imaging, etc., should help alleviate that.

we can measure uncertainty in estimates, and use photo-stimulation to activate/deactivate small groups of neurons efficiently to help reduce variance in uncertainty.

b.   y's mini-discussion   Functional connectivity may fail to faithfully represent anatomical circuit structure if false correlations are present between different neurons, induced e.g. by common inputs, or if the dynamics of neural population is entirely concentrated on a low-dimensional subspace of the full configurational space $\mathbf{n}$. Note that these two statements are, in a sense, stating the same condition: if activity of different neurons is tightly correlated, their dynamics is concentrated on a low-dimensional plane and vice-versa - concentration of dynamics onto a low-dimensional plane will be perceived as correlation in activity of different neurons. In turn, low dimensionality of the neural dynamics may be caused by different factors, including common input, small subset of command neurons driving the circuit, or even emergent property of a network. Low dimensionality of neural dynamics results in that

the inference problem becomes underdetermined, i.e. there may exist directions in $\mathbf{w}_i$ along which connectivity is not constrained by neural activity data (i.e. directions orthogonal to the subspace of all observed neural activity configurations), or is poorly constrained. This, naturally, leads to $\mathbf{w}_i$ being poorly defined along these directions. The necessary condition for good correspondence between functional connectivity weights $\mathbf{w}_i$ and anatomical connectivity, therefore, is *full-dimensionality* of the observed set of neural configurations. In case of spontaneously firing system of neurons this condition is satisfied by many neuron-firings occurring independently, thus, allowing to fully sample all possible directions in $\mathbf{w}_i$. Still, spontaneously active preparation by itself may fail to display sufficient degree of independence between firing of neurons due to low-dimensionality of observed activity space, e.g. because of emergent properties of the circuit. In that case necessary variety of independent neural activity patterns may be enforced by randomly activating subsets of neurons via ChR2 or glutamate uncaging.

We also note that the correlations induced by secondary and so on synaptic transmissions (such as when neuron A results in firing of neuron B, which in turn results in firing by neuron C), are all properly resolved in GLM-fitting process via the so called explaining-away process. In other words, because we do not just identify correlations between neural firings with the functional connectivity weights w_{ij}, but instead statistically fit a model of neural interactions, if found weights between neurons A and B, and B and C are sufficient to explain the correlation between A and C, the weight connecting A and C will not appear in the model - the correlation between A and C was "explained away" by correlations between A and B, and B and C. By this, the multi-synaptic firing patterns do not confuse our estimation process.

ADD SOME RAVINGS ABOUT PROPER/IMPROPER FUNCTIONAL CONNECTIVITY.

[1] C. Andrieu, A. Doucet, and A. Holenstein, *Particle markov chain monte carlo*, Working paper (2007).

[2] Peter Bickel, Bo Li, and Thomas Bengtsson, *Sharp failure rates for the bootstrap particle filter in high dimensions*, Pushing the Limits of Contemporary Statistics: Contributions in Honor of Jayanta K. Ghosh (Bertrand Clarke and Subhashis Ghosal, eds.), IMS, 2008, pp. 318–329.

[3] Tom Binzegger, Rodney J. Douglas, and Kevan A. C. Martin, *A Quantitative Map of the Circuit of Cat Primary Visual Cortex*, J. Neurosci. **24** (2004), no. 39, 8441–8453.

[4] S. Boyd and L. Vandenberghe, *Convex optimization*, Oxford University Press, 2004.

[5] V. Braitenberg and A. Schuz, *Cortex: statistics and geometry of neuronal connectivity.*, Springer, Berlin, 1998.

[6] D. Brillinger, *Maximum likelihood analysis of spike trains of interacting nerve cells*, Biological Cyberkinetics **59** (1988), 189–200.

[7] ———, *Nerve cell spike train data analysis: a progression of technique*, Journal of the American Statistical Association **87** (1992), 260–271.

[8] E. Buhl, K. Halasy, and P. Somogyi, *Diverse sources of hippocampal unitary inhibitory postsynaptic potentials and the number of synaptic release sites*, Nature **368** (1994), 823–828.

[9] E. J. Candes and J. Romberg, *Practical signal recovery from random projections.*, 2005.

[10] E. Chornoboy, L. Schramm, and A. Karr, *Maximum likelihood identification of neural point process systems*, Biological Cybernetics **59** (1988), 265–275.

[11] A. Dempster, N. Laird, and D. Rubin, *Maximum likelihood from incomplete data via the EM algorithm*, Journal Royal Stat. Soc., Series B **39** (1977), 1–38.

[12] D. Donoho and M. Elad, *Optimally sparse representation in general (nonorthogonal) dictionaries via L^1 minimization*, PNAS **100** (2003), 2197–2202.

[13] A. Doucet, N. de Freitas, and Gordon N., *Sequential monte carlo in practice*, Springer, 2001.

[14] A. Doucet, S. Godsill, and C. Andrieu, *On sequential Monte Carlo sampling methods for Bayesian filtering*, Statistics and Computing **10** (2000), 197–208.

[15] S. Escola and L. Paninski, *Hidden Markov models applied toward the inference of neural states and the improved estimation of linear receptive fields*, Under review, Neural Computation (2008).

[16] D. Feldmeyer, V. Egger, J. Lubke, and B. Sakmann, *Reliable synaptic connections between pairs of excitatory layer 4 neurones within a single "barrel" of developing rat somatosensory cortex*, J Physiol **521 Pt 1** (1999), 169–90.

[17] D. Feldmeyer and B. Sakmann, *Synaptic efficacy and reliability of excitatory connections between the principal neurones of the input (layer 4) and output layer (layer 5) of the neocortex*, J Physiol **525** (2000), 31–9.

[18] S.J. Godsill, A. Doucet, and M. West, *Monte Carlo smoothing for non-linear time series*, Journal of the American Statistical Association **99** (2004), 156–168.

[19] S. M. Gomez-Urquijo, C. Reblet, J. L. Bueno-Lopez, and I. Gutierrez-Ibarluzea, *Gabaergic neurons in the rabbit visual cortex: percentage, distribution and cortical projections*, Brain Res **862** (2000), 171–9.

[20] A. Gupta, Y. Wang, and H. Markram, *Organizing principles for a diversity of gabaergic interneurons and synapses in the neocortex.*, Science **287** (2000), 273–8.

[21] J. Kulkarni and L. Paninski, *Common-input models for multiple neural spike-train data*, Network: Computation in Neural Systems **18** (2007), 375–407.

[22] S. Lefort, C. Tomm, J.-C. Floyd Sarria, and C. C. H. Petersen, *The excitatory neuronal network of the c2 barrel column in mouse primary somatosensory cortex*, Neuron **61** (2009), 301–16.

[23] K. Li and N. Duan, *Regression analysis under link violation*, Annals of Statistics **17** (1989), 1009–1052.

[24] G. McLachlan and T. Krishnan, *The em algorithm and extensions*, Wiley-Interscience, 1996.

[25] Y. Mishchenko, *Strategies for identifying exact structure of neural circuits with broad light microscopy connectivity probes*, Preprint: http://precedings.nature.com/documents/2669/version/2 (2009).

[26] Y. Mishchenko, J. Spacek, J. Mendenhall, D. Chklovskii, and K. M. Harris, *Reconstruction of hippocampal ca1 neuropil at nanometer resolution reveals disordered packing of processes and dependence of synaptic connectivity on local environment and dendritic caliber.*, Preprint: http://precedings.nature.com/documents/2669/version/2 (2009).

[27] R. Neal, M. Beal, and S. Roweis, *Inferring state sequences for non-linear systems with embedded hidden Markov models*, NIPS **16** (2003).

[28] A. Ng, *Feature selection, L_1 vs. L_2 regularization, and rotational invariance*, ICML **21** (2004).

[29] D. Nykamp, *A mathematical framework for inferring connectivity in probabilistic neuronal networks*, Mathematical Biosciences **205** (2007), 204–251.

[30] L. Paninski, *Maximum likelihood estimation of cascade point-process neural encoding models*, Network: Computation in Neural Systems **15** (2004), 243–262.

[31] L. Paninski, M. Fellows, S. Shoham, N. Hatsopoulos, and J. Donoghue, *Superlinear population encoding of dynamic hand trajectory in primary motor cortex*, J. Neurosci. **24** (2004), 8551–8561.

[32] C. C. Petersen and B. Sakmann, *The excitatory neuronal network of rat layer 4 barrel cortex*, J Neurosci **20** (2000), no. 20, 7579–86.

[33] J. Pillow, J. Shlens, L. Paninski, A. Sher, A. Litke, E.J. Chichilnisky, and E. Simoncelli, *Spatiotemporal correlations and visual signaling in a complete neuronal population*, Nature **454** (2008), 995–999.

[34] H. Plesser and W. Gerstner, *Noise in integrate-and-fire neurons: From stochastic input to escape rates*, Neural Computation **12** (2000), 367–384.

[35] L. Rabiner, *A tutorial on hidden Markov models and selected applications in speech recognition*, Proceedings of the IEEE **77** (1989), 257–286.

[36] A. Reyes, R. Lujan, A. Rozov, N. Burnashev, P. Somogyi, and B. Sakmann, *Target-cell-specific facilitation and depression in neocortical circuits*, Nat Neurosci **1** (1998), 279–285.

[37] F. Rigat, M. de Gunst, and J. van Pelt, *Bayesian modelling and analysis of spatio-temporal neuronal networks*, Bayesian Analysis **1** (2006), 733–764.

[38] R. J. Sayer, M. J. Friedlander, and S. J. Redman, *The time course and amplitude of epsps evoked at synapses between pairs of ca3/ca1 neurons in the hippocampal slice*, J. Neurosci. **10** (1990), 826–36.

[39] R. Shumway and D. Stoffer, *Time series analysis and its applications*, Springer, 2006.

[40] S. Song, P. J. Sjostrom, M. Reigl, S. Nelson, and D. B. Chklovskii, *Highly nonrandom features of synaptic connectivity in local cortical circuits.*, PLoS Biology **3** (2005), e68.

[41] I. Stevenson, J. Rebesco, N. Hatsopoulos, Z. Haga, L. Miller, and K. Koerding, *Inferring network structure from spikes*, Statistical Analysis of Neural Data meeting (2008).

[42] I. H. Stevenson, J. M. Rebesco, N. G. Hatsopoulos, Z. Haga, L. E. Miller, and K. P. Kording, *Bayesian inference of functional connectivity and network structure from spikes*, IEEE Trans. Neural Systems and Rehab. **17** (2009), 203–13.

[43] A. Thompson, D. Girdlestone, and D. West, *Voltage-dependent currents prolong single-axon postsynaptic potentials in layer III pyramidal neurons in rat neocortical slices*, J Neurophysiol **60** (1988), 1896–1907.

[44] R. Tibshirani, *Regression shrinkage and selection via the lasso*, Journal of the Royal Statistical Society. Series B **58** (1996), 267–288.

[45] M. Tipping, *Sparse Bayesian learning and the relevance vector machine*, Journal of Machine Learning Research **1** (2001), 211–244.

[46] W. Truccolo, U. Eden, M. Fellows, J. Donoghue, and E. Brown, *A point process framework for relating neural spiking activity to spiking history, neural ensemble and extrinsic covariate effects*, Journal of Neurophysiology **93** (2005), 1074–1089.

[47] M. Vidne, J. Kulkarni, Y. Ahmadian, J. Pillow, J. Shlens, E. Chichilnisky, E. Simoncelli, and L. Paninski, *Inferring functional connectivity in an ensemble of retinal ganglion cells sharing a common input*, COSYNE (2009).

[48] J. T. Vogelstein, B. O. Watson, A. M. Packer, R. Yuste, B. Jedynak, and L. Paninski, *Spike inference from calcium imaging using sequential monte carlo methods*, Preprint (2009).

[49] R. Yasuda, E. A. Nimchinsky, V. Scheuss, T. A. Pologruto, T. G. Oertner, B. L. Sabatini, and K. Svoboda, *Imaging calcium concentration dynamics in small neuronal compartments*, Sci STKE **219** (2004), p15.
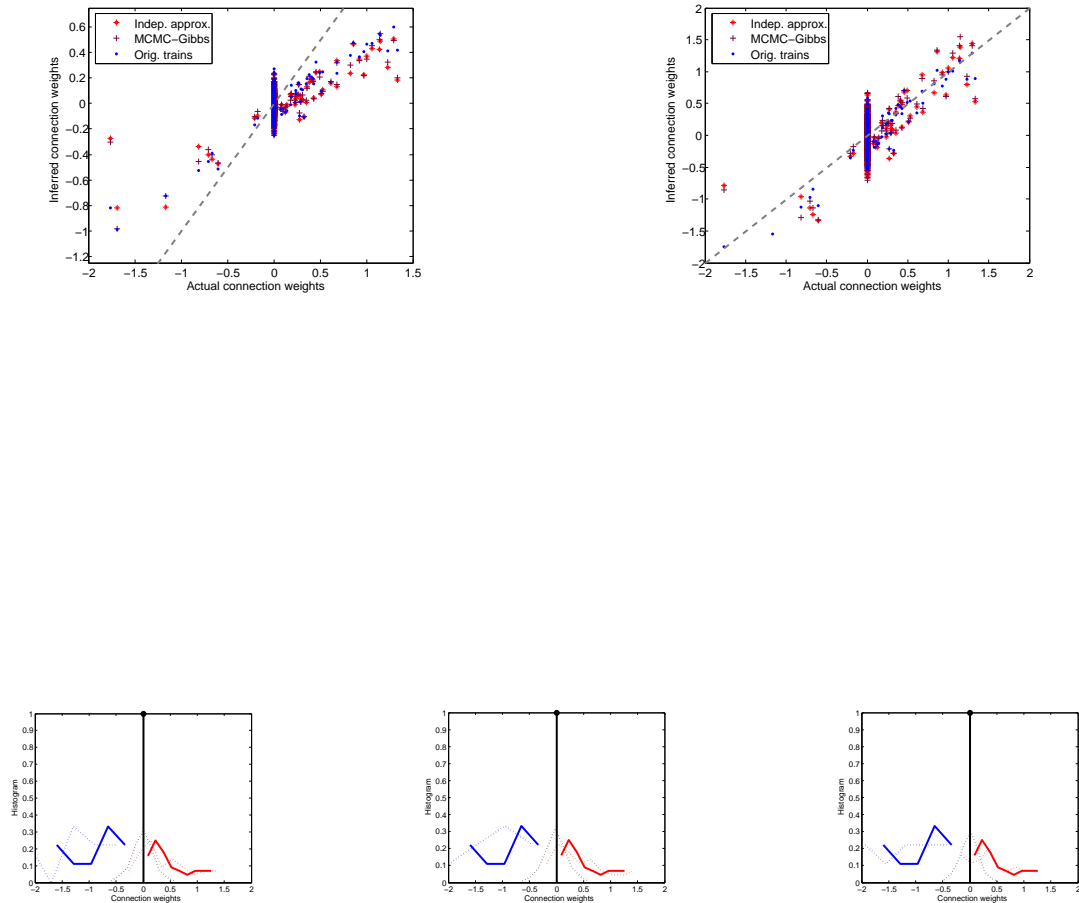
FIG. 3: Functional connectivity matrix can be reconstructed from calcium imaging data. In the upper panels inferred connection weights are shown in a scatter plot versus real connection weights, with inference performed using independent approximation algorithm, exact MCMC-Gibbs algorithm, and original spike trains observed at the frame-rate of the calcium imaging. Network of $N = 25$ neurons was used, firing at 5 Hz, and imaged for T=600 sec at intermediate SNR (photon budget 10Kph/neuron/frame, see below). $r^2 = 0.47$ for independent approximation algorithm was found, $r^2 = 0.48$ for MCMC-Gibbs algorithm, and $r^2 = 0.57$ for the original spike trains. Thus, independent approximation produced results almost as accurate as the exact MCMC-Gibbs algorithm, and almost as accurate as the original spikes. Inferred connectivity weights (upper left) were scaled with respect to true connectivity by a constant amount due to time discretization bias (see below); other than scale, inferred connectivity represented the true connectivity matrix very well (upper right). Lower panels show the inferred histograms of the connection weights (dotted lines) versus that of the true connectivity matrix (think solid lines). Blue corresponds to negative (inhibitory) connections, red corresponds to positive (excitatory) connections, and black corresponds to zero (absent) connections in the true connectivity matrix. Thus, calcium imaging is sufficient to identify connected pairs of neurons reliably.
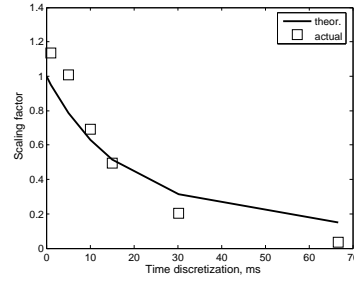
FIG. 4: Low-frame rate of calcium imaging, leading to large bin size $\Delta \approx 15 - 30$ ms of the inferred spike trains, is the reason of scaling bias in the estimated connectivity matrix. This bias is explained well by considering what number of causally-related spikes from a pair of neurons are delayed by Δ or more, and so their temporal order can be reliably determined from calcium imaging data.
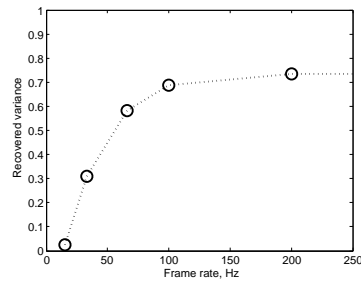

FIG. 5: Accuracy of the inferred connectivity weights as function of the frame rate of calcium imaging. Connectivity matrix here was inferred from the original spike trains observed at corresponding frame-rates, thus establishing the upper performance bound for inference using calcium imaging data. A network of $N = 25$ neurons, firing at 5 Hz and imaged for $T = 600$ sec was used.
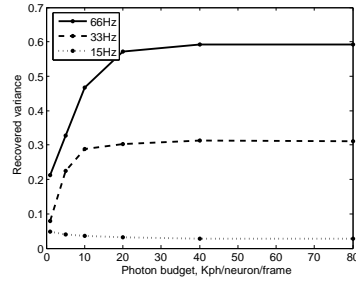
FIG. 6: Accuracy of inferred connectivity weights as function of the noise amount in the calcium imaging data, as quantified by experimental photon budget per neuron-frame, for frame rates of 15 Hz, 33 Hz and 66 Hz. Photon counts on the order of 20-40 Kph/frame/neuron are required to achieve the upper bound due by the frame-rate. Connectivity matrix here was inferred from simulated fluorescence data using independent approximation algorithm. A network of $N = 25$ neurons, firing at 5 Hz and imaged for $T = 600$ sec was used.
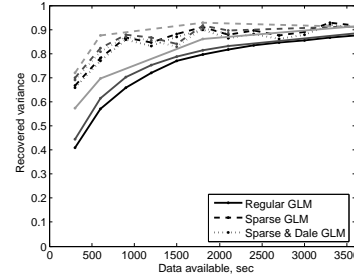
FIG. 7: Accuracy of inferred connectivity weights as function of the imaging time and neural population size. Incorporating simple priors such as exponential prior on the connectivity weights allows to boost reconstruction accuracy dramatically (dashed lines). In this latter case, $T = 300$ sec is already sufficient to recover 70% of the variance in the connection weights. Incorporating Dale's prior leads to only marginal improvement (dotted line). As shown in the methods, reconstruction accuracy does not depend on the neural population size N (gray lines - light gray lines are for neural population size of $N = 200$ neurons, dark gray line are for $N = 100$ neurons and black lines are for $N = 50$ neurons). $T = 5$ min - 0.5 hour is sufficient to produce accurate reconstructions.
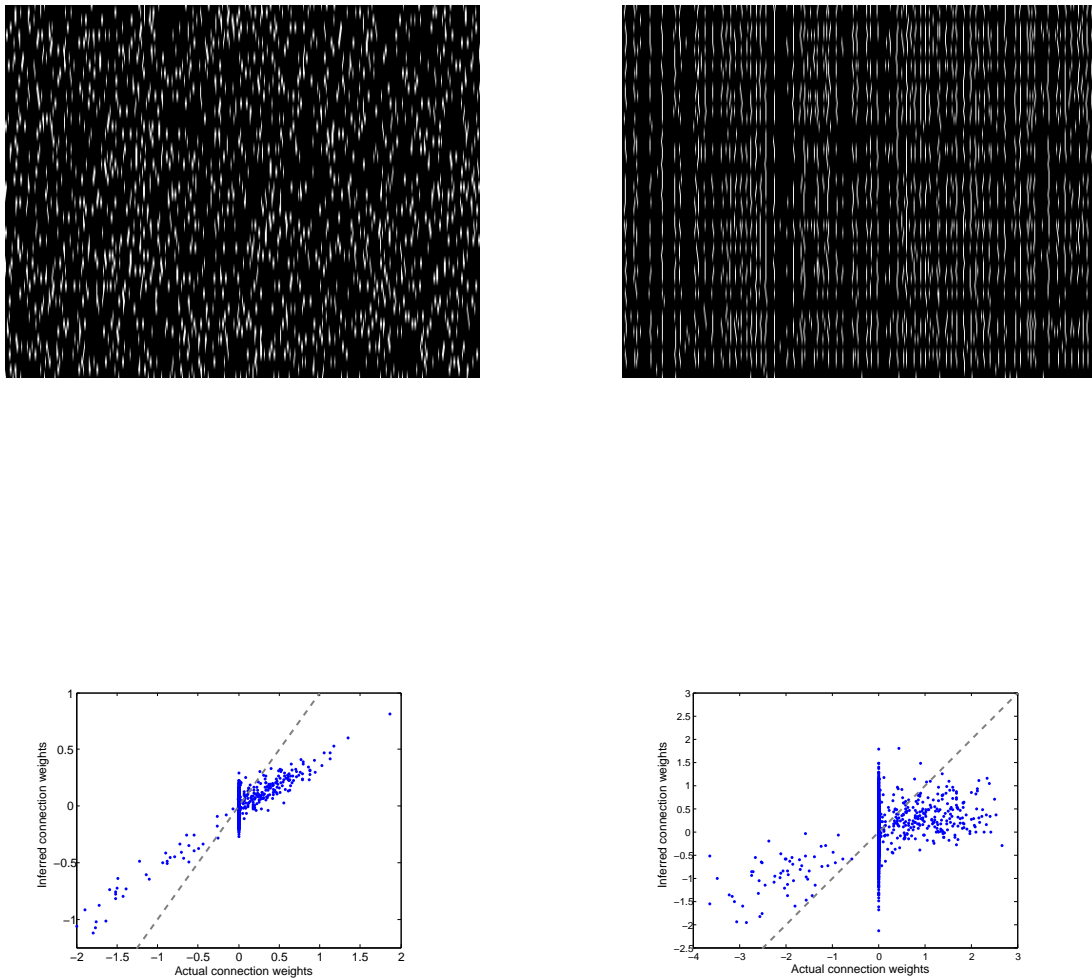
FIG. 8: Diverseness of observed neural activity patterns is required for functional connectivity to give access to the actual "anatomical" structure of the neural circuit. Here, 15 sec of simulated spike trains for a weakly coupled network (upper-left) and a network with strongly coupled component (upper-right) are shown. In weakly coupled network spikes are sufficiently uncorrelated to give access to all different neural activity patterns needed to properly estimate true weights $\mathbf{w}_i$. In strongly coupled case, many instances of highly synchronous locked firings are evident, thus preventing observation of sufficiently rich ensemble of activity patterns. Accordingly, GLM solution for the strongly coupled neural network (lower-right) does not represent the true connectivity of the circuit, even for the weakly coupled circuit's component. This is contrary to the weakly-coupled network (lower-left) where true connectivity is successfully estimated.
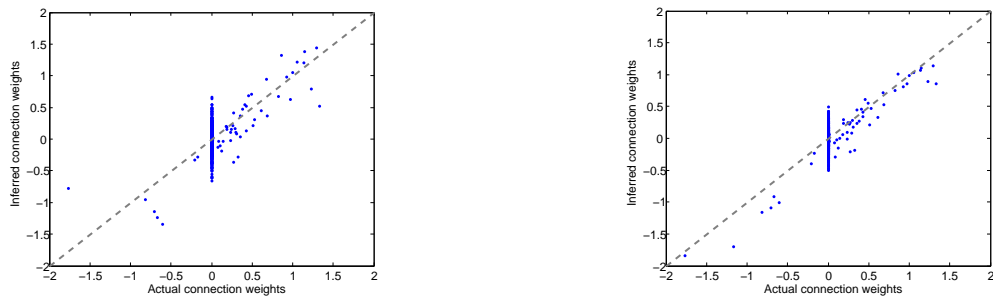
FIG. 9: Bayesian inference algorithm is robust to distortions of the underlying generative model. One distortion that should be expected is variability of the EPSP time courses from neuron to neuron, and possibly synapse to synapse. With up to 25% variability allowed in EPSP time scales τ_w (right panel) our algorithm provided reconstructions of the same quality as when all τ_w were the same (left panel).
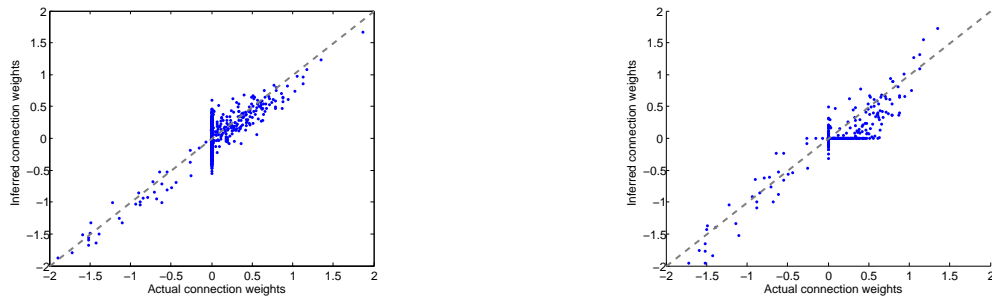
FIG. 10: Incorporating simple priors on the distribution of connectivity weights in the Bayesian inference algorithm, such as exponential sparseness prior, is essential to achieve much more accurate reconstructions than using simple GLM from a smaller amount of calcium imaging data. Here, connection weights reconstructed using simple GLM (left panel) or sparse-prior GLM (right panel) are shown in a scatter plot for a network of $N = 50$ neurons firing at 5 Hz and imaged for T=600 sec. $r^2 = 0.64$ for simple GLM solution and $r^2 = 0.85$ for sparse-GLM solution.
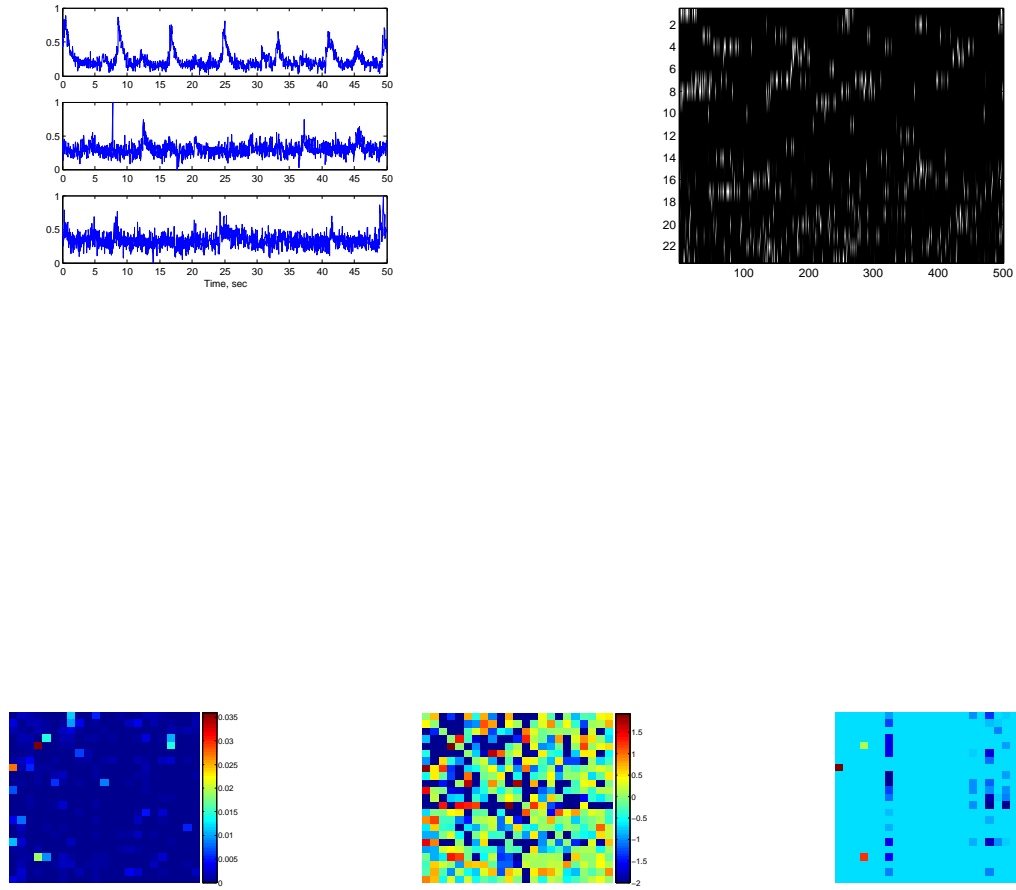
FIG. 11: Functional connectivity matrix inferred from a sample of actual calcium imaging data for $N = 72$ cells in [XXX], imaged for $T \approx 260$ sec at 15 Hz. $N = 23$ neurons with spikes at sufficient SNR were selected, and functional connectivity reconstructed using independent approximation algorithm. Firing cell of these cells was 0.1-1 Hz and 20-200 spikes were collected for each neuron. Upper-left panel shows example of actual fluorescence traces from selected cells, best to worst. Upper-right panel shows a raster of inferred spike trains for first 100 sec of imaging data. Lower panels show left-to-right the time-delayed cross-correlation matrix for selected neurons, simple GLM solution and sparse GLM solution, respectively. A consistent connectivity matrix is obtained here, with sparse solution having sparseness of $\approx 10\%$, and all neurons automatically respecting Dale's law without explicitly enforcing it. Two clearly excitatory, and three clearly inhibitory neurons can be seen, with remaining neurons not showing significant couplings.